The Astrophysical Journal, 1011:111 (13pp), 2026 November 1 https://doi.org/10.3847/1538-4357/aeb1a6
© 2026. The Author(s). Published by the American Astronomical Society.
OPEN ACCESS

Collective Vortex Dynamics: From Isolated Vortices to Their Communities

Lauren McClure[1], Suzana Silva[1], Gary Verth[2], Istvan Ballai[2], and Viktor Fedun[1]
[1] Plasma Dynamics Group, School of Electrical and Electronic Engineering, The University of Sheffield, Sir Frederick Mappin Building, Mappin Street, Sheffield, S1 3JD, UK
[2] Plasma Dynamics Group, School of Mathematical and Physical Sciences, The University of Sheffield, Hicks Building, Hounsfield Road, Sheffield, S3 7RH, UK
Received 2026 March 18; revised 2026 October 6; accepted 2026 October 6; published 2026 October 29

Abstract

Small-scale vortical motions in the upper solar atmosphere are abundant and occupy about 2.8% of the photosphere at any given time. Although considerable work has focused on the detection and analysis of individual solar vortices, the interconnected and multiscale behaviour of these coherent structures remains largely unexplored. We present a methodology for studying this behaviour through vortex interactions to improve our understanding of how small- and large-scale photospheric flows contribute to energy transfer into the upper solar atmosphere and to the driving of solar activity. We represent vortices as a network of interacting structures. We apply a community detection algorithm to derive an optimal reduced network composed of highly interconnected vortex groups. From the interaction patterns and group structure, we define three roles within each community: peripheral, connector, and hub. We then track both vortex communities and their member vortices from the photosphere into the chromosphere and across their lifetimes. On average, vortices assigned to these roles persist to greater heights in the chromosphere and have longer lifetimes than unclassified vortices. This shows that community detection can identify vortices with greater dynamical influence on the upper solar atmosphere. We also find that 36.4%–59.5% of vortex communities exhibit global periodic behaviour following a helical path. This collective vortical motion may indicate an enhanced mechanism for wave excitation. Solar vortical community detection, therefore, offers a new framework for studying solar vortices and a new perspective on the importance of collective vortex dynamics.

Unified Astronomy Thesaurus concepts: Solar physics (1476); Solar atmosphere (1477); Solar photosphere (1518); Solar chromosphere (1479)

1. Introduction

Vortical motions are observed throughout the solar atmosphere, from photospheric vortices to large-scale chromospheric swirls and tornados (S. Wedemeyer-Böhm et al. 2012; K. Tziotziou et al. 2023), and have been proposed to transport energy (N. Yadav et al. 2020; H. Kuniyoshi et al. 2023; S. S. A. Silva et al. 2024a, 2024b), mass, and momentum into the upper atmosphere, with implications for coronal heating and solar wind acceleration (F. P. Zuccarello et al. 2017; A. Finley et al. 2022; K. Tziotziou et al. 2023). Characterizing their dynamics is therefore important for understanding upper atmospheric energetics, though quantifying small-scale vortex effects remains challenging given their abundance and complex dynamics (I. Giagkiozis et al. 2018). Much of the solar vortex literature focuses on determining vortex sizes, lifetimes, occurrence rates, and associated energy and transport estimates (R. Moll et al. 2011; S. Shelyag et al. 2011; S. Vargas Domínguez et al. 2011; I. Giagkiozis et al. 2018; K. Tziotziou et al. 2018; Y. Aljohani et al. 2022; L. McClure et al. 2026), with many studies also examining connections to wave excitation, magnetic concentrations, and localized heating (S. Wedemeyer-Böhm et al. 2012; K. Tziotziou et al. 2023; H. Kuniyoshi et al. 2025). However, these works predominantly examine vortices as individual features rather than as members of dynamically interacting populations. While this perspective can be appropriate for isolated structures, this is not the case for photospheric vortices, considering they appear largely in groups (I. Giagkiozis et al. 2018; S. S. A. Silva et al. 2020) and can therefore interact collectively, generating larger-scale dynamics. To address this aspect, we introduce a community detection framework that identifies coherent, interacting vortex groups from an interaction network. This enables community-level observables and a new view of collective dynamics.

Network science reduces complex systems into group dynamics (M. Newman 2010), with modularity maximization partitioning networks based on node interactions (M. E. J. Newman & M. Girvan 2004; M. E. J. Newman 2006). This approach has been widely applied across neuroscience (D. S. Bassett et al. 2011), economics (M. MacMahon & D. Garlaschelli 2015), and biological networks (A. C. F. Lewis et al. 2010). In hydrodynamics, network and graph-theoretic methods have been applied to turbulent vortex systems and unsteady aerodynamic modeling (A. G. Nair & K. Taira 2015; K. Taira et al. 2016; M. Gopalakrishnan Meena et al. 2018). A. G. Nair & K. Taira (2015) introduced a vortex network representation where interaction strength is defined via induced velocity, consistent with the Biot–Savart formulation (P. G. Saffman 1992). Treating vortices as interacting structures rather than isolated features has advanced our understanding of vortex-driven systems. One of the first explicit community detection frameworks for vortical flows was proposed by M. Gopalakrishnan Meena et al. (2018). They showed that macroscopic hydrodynamic dynamics can be captured using a reduced description based on vortex communities. Their approach enables the prediction of selected observables and is reported to be robust to noise and turbulent variability. Building on this, M. Gopalakrishnan Meena & K. Taira (2021) classified vortices and communities according

Original content from this work may be used under the terms of the Creative Commons Attribution 4.0 licence. Any further distribution of this work must maintain attribution to the author(s) and the title of the work, journal citation and DOI.

to their intracommunity and intercommunity interactions. They found that the network-based categories align with distinct physical flow characteristics.

Vortical community detection remains a relatively new development, yet it has already provided insights into the global dynamics of turbulent systems and demonstrated a new research direction in hydrodynamics (K. Taira et al. 2016; M. Gopalakrishnan Meena et al. 2018). The vortical community approach provides a scalable framework for identifying groups of vortices that interact and evolve together within a large and complex system (M. Gopalakrishnan Meena et al. 2018). Applied to solar atmospheric flows where vortices are abundant, vortex community detection could reveal whether populations of small-scale interacting vortices can organize larger, mesogranular-scale patterns of motion, thereby influencing how energy is transported and redistributed through the solar atmosphere. Extending these techniques to magnetohydrodynamic environments, however, introduces additional challenges, including compressibility effects, magnetic forces, and the need to account for the full three-dimensional structure of solar vortical flows (E. Priest 2014).

We introduce a solar vortical community detection framework, applying it to simulated quiet-Sun data spanning the photosphere to chromosphere (B. V. Gudiksen et al. 2011). By constructing a vortex interaction network, we identify dynamically influential vortices and link them to distinct physical properties. We then apply modularity maximization to detect coherent vortex communities, revealing how their structure relates to collective motion evolving across time and atmospheric height

2. Methodology

2.1. Bifrost Simulation Data

The dataset used in this study was generated with the multidimensional radiative magnetohydrodynamics code Bifrost (B. V. Gudiksen et al. 2011), which simulates realistic photospheric velocity and magnetic fields. In this paper, we use the simulation "ch024031_by200bz005," which simulates coronal hole conditions and is publicly available through the Hinode Science Data Center. Further details of the simulation setup are given by B. V. Gudiksen et al. (2011), M. Carlsson et al. (2016), and A. Finley et al. (2022).

We analyze the full horizontal extent of the simulation (24×24 Mm) at a horizontal resolution of 31 km (M. Carlsson et al. 2016; A. Finley et al. 2022). The analysis uses a continuous ≈37 minute time series (indices 249–469) sampled every 10 s. The vertical grid is nonuniform, and we consider heights from ≈0.45 Mm above the solar surface (photospheric layers) up to ≈2 Mm to assess vortex tube heights and coherent structures extending into the upper atmosphere. We choose the initial height of ≈0.45 Mm because vortical structures are larger than in the lower photosphere and thus better resolved by the horizontal grid, improving the robustness of community detection.

Across this interval, the vertical spacing varies between 12.35 and 12.7 km. The high spatial resolution and cadence make the dataset well suited for studying and tracking small-scale turbulent motions such as solar vortices. Figure 1 shows the actual horizontal velocity field over the full simulation domain at the initial analyzed time and photospheric height, with the detected vortex centers overlaid.

2.2. Vortex Interactions

In this work, we apply a community detection algorithm to systems of solar vortices (M. E. J. Newman 2006; V. D. Blondel et al. 2008). Similar frameworks have been employed to hydrodynamic point-vortex systems (an idealized, two-dimensional flow model in which all vorticity is concentrated at a single point with finite circulation) by A. G. Nair & K. Taira (2015), K. Taira et al. (2016), and M. Gopalakrishnan Meena et al. (2018). They demonstrated that community-based modeling can capture aspects of global flow evolution and provide a route toward predicting collective motion and observable signatures. Here, we extend this concept to a magnetohydrodynamic setting by detecting vortices in the Bifrost simulation described in Section 2.1 using the Γ method (L. Graftieaux et al. 2001). We adopt a dual Γ approach with dynamic thresholding to reduce false positives and to track vortices more robustly across their full spatial and temporal extent. Similar to the study by L. McClure et al. (2026), we apply a normalization preprocessing step. All vortex detection details used in this work are reported in Appendix A.

We quantify the rotational strength enclosed by the detected boundary of vortex i through its circulation,

$$\gamma_i = \sum_{V_i} \omega_z \Delta A, \tag{1}$$

where V_i denotes the region enclosed by the boundary of the ith vortex, ω_z is the vertical component of vorticity, and ΔA is the area of a grid cell.

The circulation, γ_i, is then used to define the velocity induced by vortex i to vortex j ($i \neq j$) as

$$u_{i\to j} = \frac{\gamma_i}{2\pi|\boldsymbol{r}_j - \boldsymbol{r}_i|}, \tag{2}$$

where $\boldsymbol{r}_i$ and $\boldsymbol{r}_j$ denote the horizontal positions of vortex centers (P. G. Saffman 1992; A. G. Nair & K. Taira 2015; M. Gopalakrishnan Meena et al. 2018). For $i = j$, we set $u_{i\to j} = 0$ in all subsequent calculations as self-induction is undefined within this two-dimensional vortex interaction formulation. In this approach, γ_i scales with the horizontal area enclosed by the detected vortex boundary, implying that the induced velocity is sensitive to the chosen boundary definition.

The velocity induced by one vortex on another depends on their relative positions. By translating the coordinate system so that a source vortex is located at the origin, its induced velocity can be expressed at any point in the surrounding flow. In this induced field, streamlines form concentric circles centered on the vortex. Using polar coordinates with vortex i's center point as $r_i = 0$, the contribution from one vortex to the total induced velocity is

$$\boldsymbol{u}_i(r) = \frac{\gamma_i}{2\pi r}\,\hat{\phi}. \tag{3}$$

The flow speed is uniform along each circle but varies between circles, and the motion is purely tangential, with no radial component (P. G. Saffman 1992). Applying this construction to all vortices in the domain yields the total induced velocity field, which represents the collective influence of the vortex population on the surrounding flow. A visualization of this field is shown in the top two main panels of Figure 2. The black streamlines in these panels illustrate the total induced velocity field, highlighting the net dynamical influence of

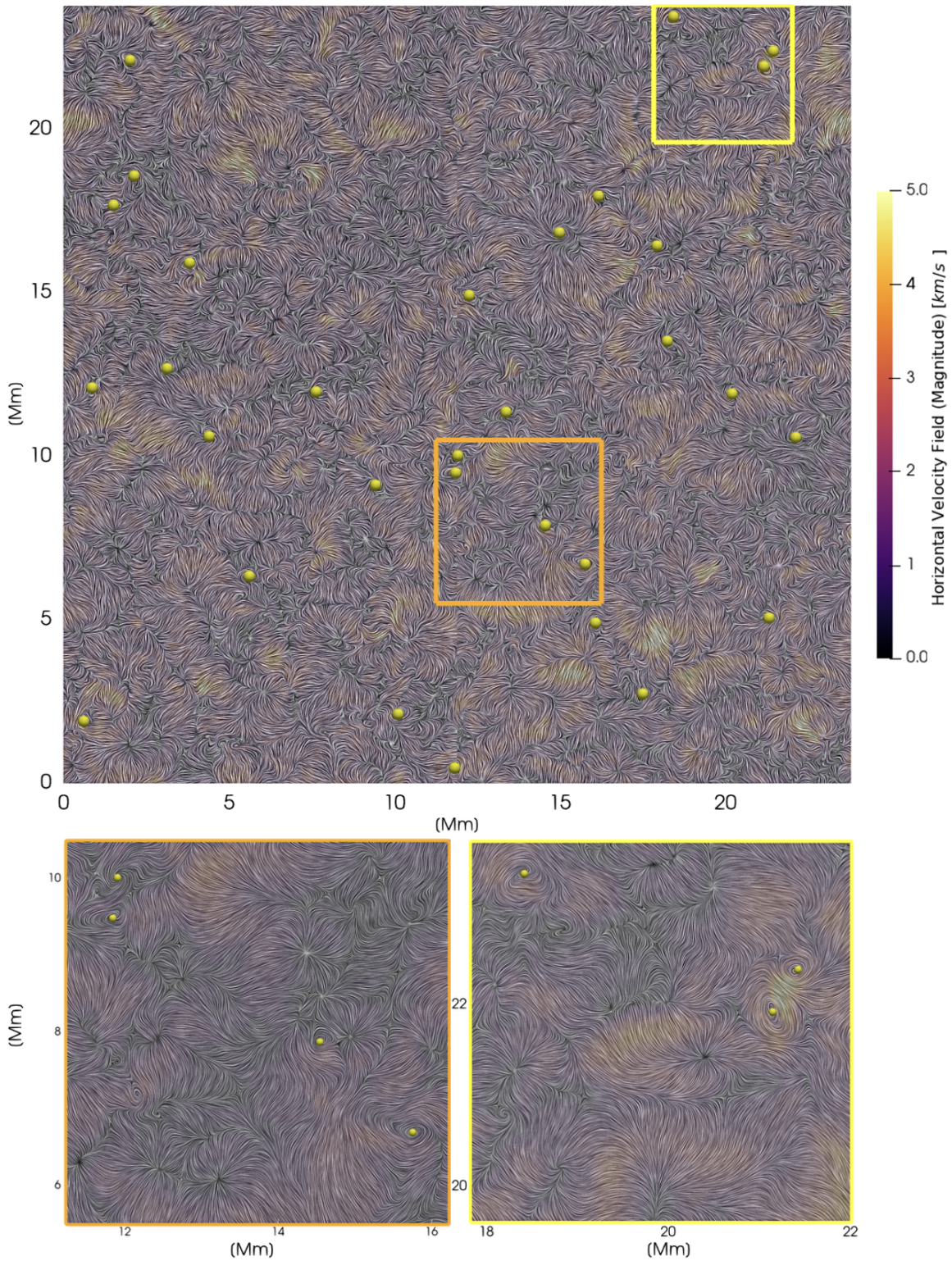


Figure 1. Horizontal velocity field over the full simulation domain at $t = 0$ and a photospheric height of approximately 0.45 Mm. The line integral convolution texture indicates the local flow direction (B. Cabral & L. C. Leedom 1993), while the background color represents the horizontal velocity field magnitude. Yellow markers denote the detected vortex centers. We highlight two zoomed-in views to show the swirling velocity fields around the centers.

individual vortices. We also present the induced velocity magnitude and its angular deviation from the actual velocity vector. To aid comparison between the two fields, the corresponding actual horizontal velocity field at the same time and height is shown in Figure 1. Regions surrounding vortex centers show strong directional agreement between these fields, and the vortex's region also naturally coincides (see Equation (2)) with the locations of the largest induced velocity magnitude. Note that the induced velocity derives from detected vortices only, so undetected vortices may

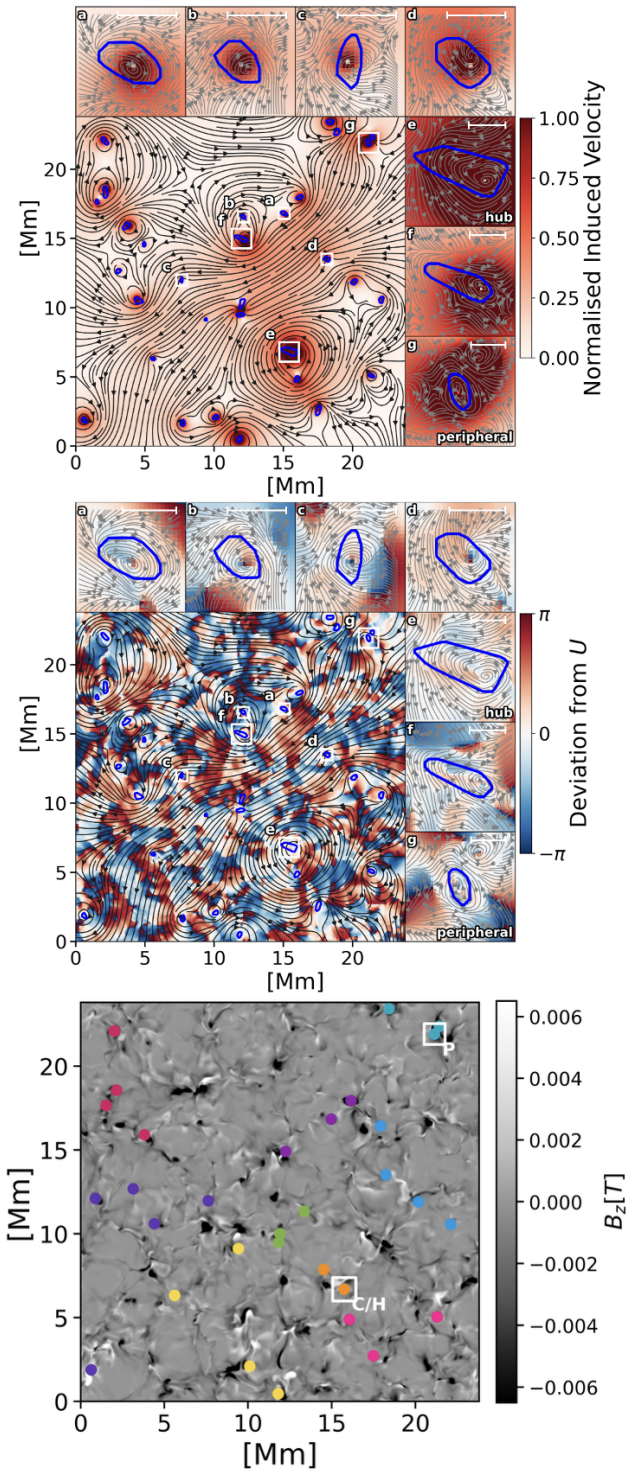


Figure 2. Vortex detection results over the full field of view at $t = 0$ s. Black streamlines in the top two panels show the total induced velocity field, computed from the contributions of all detected vortices, while panels (a)–(g) show streamlines in gray of the actual velocity fields. The white scale bar denotes 0.5 Mm. Panels (e) and (g) highlight the hub and peripheral vortices at this time frame. The top main panel shows the normalized induced velocity magnitude, and the middle main panel shows the angle (in radians) between the velocity field (U) and induced velocity vectors. The community structure is shown in the bottom panel on a background of the z-component of the magnetic field, where marker color denotes community membership. The highlighted centers labeled P, C, and H identify the peripheral, connector, and hub vortices, respectively, for this time frame.

introduce discrepancies reflecting detection limitations. Given the requirements on vortex strength by the gamma method, any missed vortices are expected to be smaller and rotationally weaker than those detected, meaning their circulation and contribution to the total induced velocity field would likely be small.

The induced velocity interactions, however, provide a natural framework for representing the vortex population as a dynamically connected system rather than a collection of isolated features. We construct an interaction network based on these induced velocities and apply modularity maximization to identify community structures within the vortex population. We present an example of a community structure for our data in Figure 3(a) (M. E. J. Newman 2006; M. Gopalakrishnan Meena et al. 2018). The network partition is obtained using an iterative Louvain method applied to the induced velocity connectivity (V. D. Blondel et al. 2008). This approach reveals groups of vortices that are preferentially interconnected and enables a classification of vortices according to their structural role within the community structure.

Using this framework, we define three classes of influential vortices in the network: hub, peripheral, and connector vortices (M. Gopalakrishnan Meena & K. Taira 2021). In the induced velocity network, a hub vortex contributes the largest share of the induced velocity and is typically the most influential vortex in the system. Figure 2 illustrates this behavior for the hub vortex (tile (e) in the top panels), which produces the strongest local distortion of the surrounding streamlines.

Peripheral vortices, in contrast, generate the largest induced velocity within their own community but belong to groups that have relatively weak intercommunity interaction in the reduced network. As a result, they exert a strong local influence while contributing less to the global network dynamics. In Figure 2, the peripheral vortex (tile (g) in the top panels) is located within the cluster in the upper-right region, where the associated streamlines indicate that the induced flow remains largely confined to the Local Group.

Connector vortices, in contrast, are associated with strong interactions that extend across multiple communities (M. Gopalakrishnan Meena & K. Taira 2021). They are characterized by high intracommunity connectivity within their own group while simultaneously maintaining comparatively strong intercommunity links. As a result, connector vortices play an important role in mediating interactions between otherwise weakly coupled communities. In the bottom panel of Figure 2, we highlight the peripheral, connector, and hub vortices identified at $t = 0$. At this time step, a single vortex is assigned both the connector and hub roles, indicating that it simultaneously satisfies the criteria for both classifications.

3. Results

3.1. Lifetimes of Photospheric Vortices and Vortex Communities and Temporal Behavior

Using the dual-part Γ method described in Appendix A, we analyzed the full domain at a fixed photospheric height of $\approx$0.45 Mm and identified more than 1000 coherent vortices. These vortices were tracked across 220 frames, with lifetimes

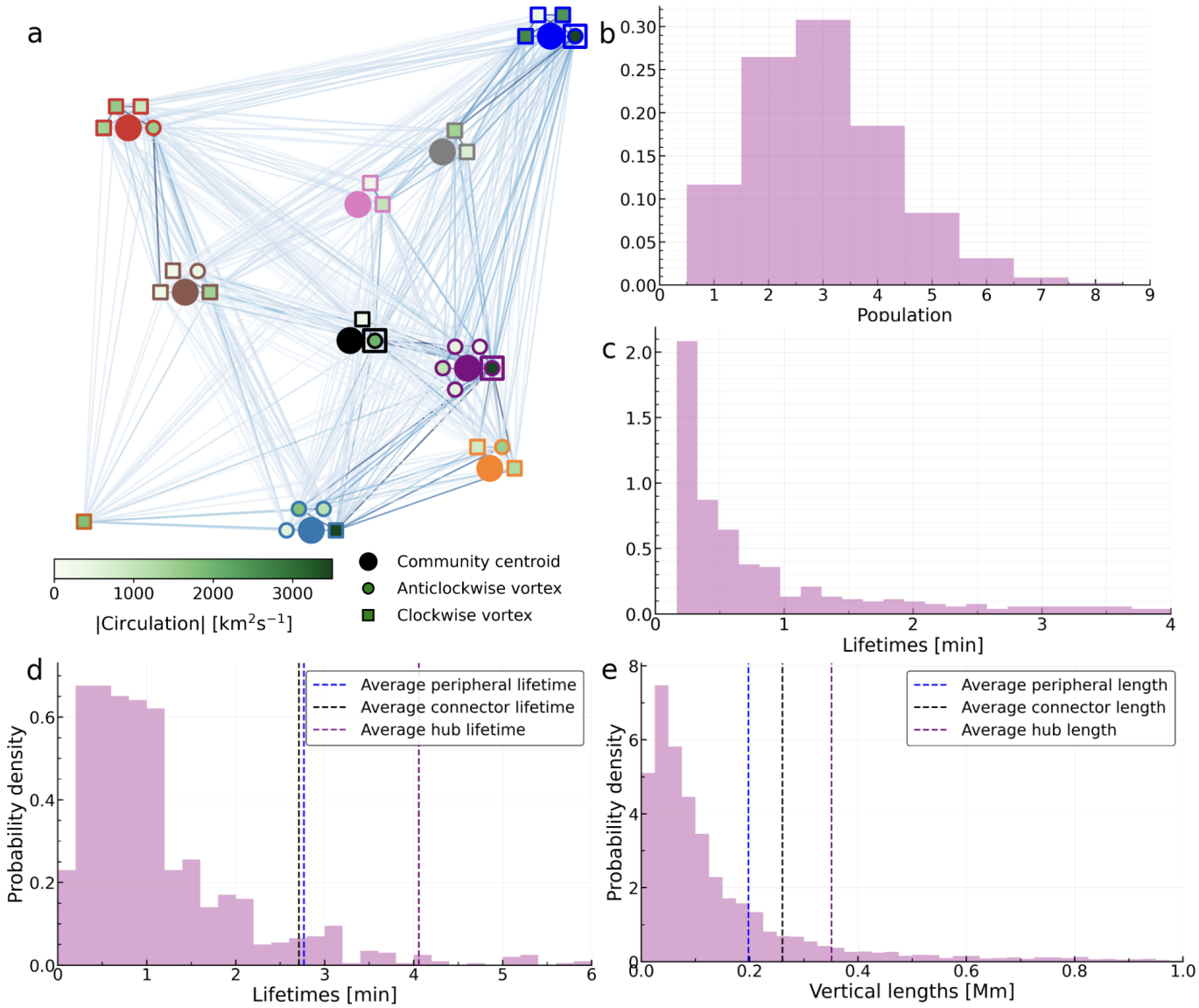


Figure 3. We present, in panel (a), an example community structure, where the centroid colors and vortex border color indicate community membership, with each centroid surrounded by its member vortices. Marker faces are colored by $|\gamma_i|$. Vortices are linked by lines colored by the mean induced velocity magnitude between each pair, with darker colors corresponding to higher values. Boxes highlight the peripheral, connector, and hub (blue, black, and purple). Histograms of property distributions for vortex communities (panels (b), (c)) and individual vortices (panels (d), (e)). Panels (b) and (c) show community size and duration. Panel (e) shows vortex tube length, and panel (d) shows vortex lifetime truncated to 6 minutes; the full range can be seen in Figure C1. The histograms are plotted as probability densities, such that the area of each bar represents the fraction of the total population within that bin; equivalently, the height of each bar is the population fraction divided by the bin width. The total area under each histogram is therefore normalized to unity. Panels (d) and (e) are revisited in Figures C1 and C2, where the smoothed probability density distributions for each class are presented and compared with the probability density distribution for the full data.

recorded only for vortices that both formed and fully dissipated within the analyzed time series.

Over the same period, we identified and tracked 340 distinct vortex communities at ≈0.45 Mm above the solar surface. Each community represents a group of vortices connected through induced velocity interactions. These communities vary in both size and composition and may either be detected instantaneously or persist across multiple time frames. For the vortex-class statistics, each vortex contributes only one entry to its assigned class, even if that classification persists over multiple frames. In Figure 3, we report the distributions of community population (b), defined as the number of vortices in each community, and community duration (c). These distributions describe the optimum reduced network structure inferred from vortex interactions.

We define the end of a community's lifetime as the time step at which none of its constituent vortices remains assigned to that community. This may occur either because the vortices migrate to other communities or because they dissipate. As shown in Figure 3(d), peripheral, connector, and hub vortices all have longer mean detected lifetimes than the full vortex population. The mean lifetimes are 2.77 minutes for peripheral vortices, 2.71 minutes for connector vortices, and 4.1 minutes for hub vortices, compared with 1.18 minutes for the full sample. These mean values are computed only from vortices that fully dissipate within the analyzed time series.

Figure 4 presents examples of vortex evolution over time (a, b, c, and g). The individual vortex tracks shown in panels (a), (b), and (c) correspond to representative peripheral, connector, and hub vortices, respectively. Circulation is displayed at each

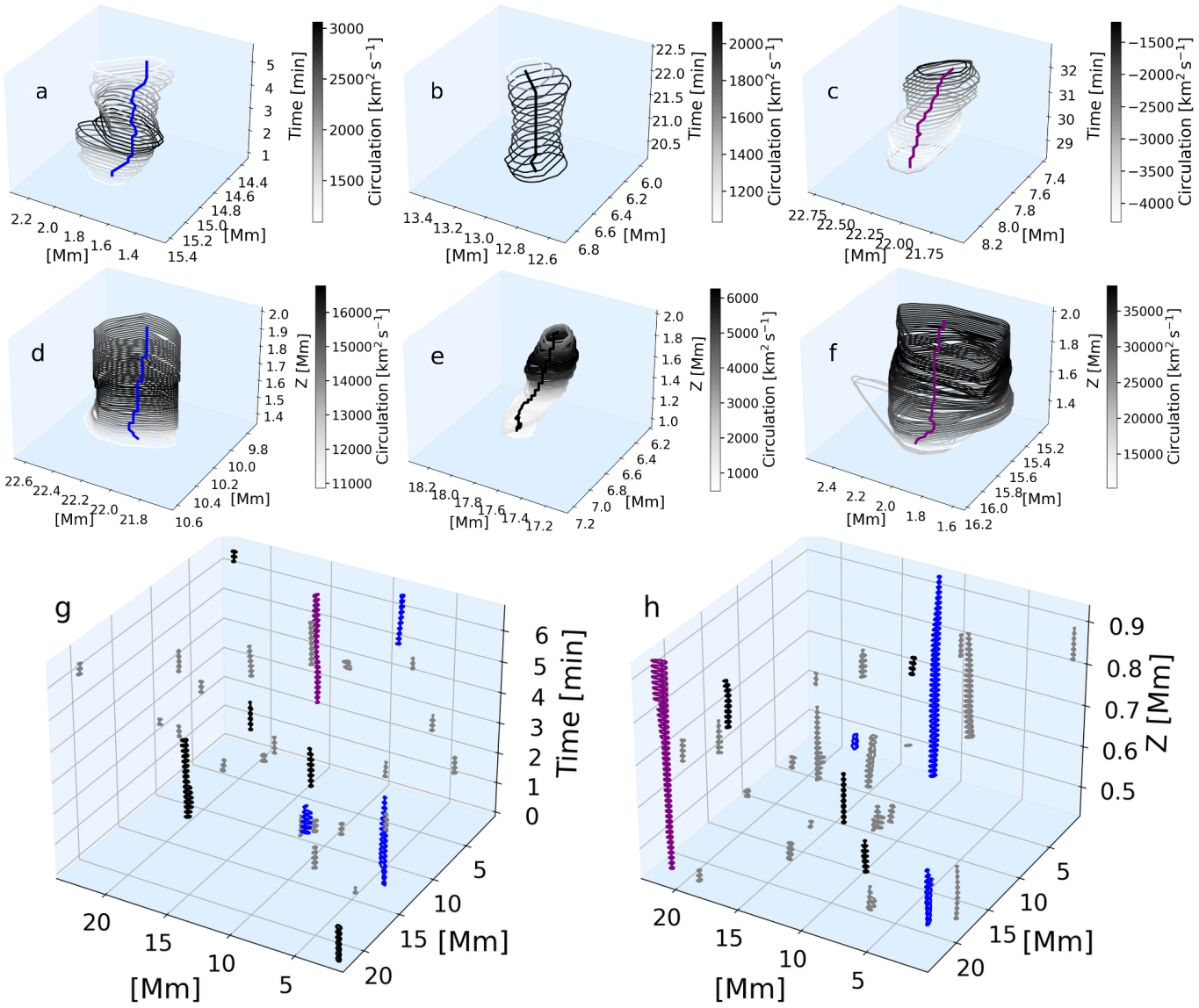


Figure 4. Examples of vortex detections over their lifetime or vertical extent. Figures (a)–(f) show individual vortex detections, where the boundaries throughout their lifetime or height range are colored by the circulation at that time/height. For these panels, the detected center is colored by vortex role—blue for peripheral, black for connector, and purple for hub. This color scheme is also used in figures (g) and (h) to represent the classified vortices, in which gray is any vortex that does not fall into any of the three classes. Panels (g) and (h) show a subset of detected vortices at different times or heights.

time step to illustrate variations in rotational strength during the vortex evolution and decay. The peripheral vortex in panel (a) begins with relatively weak circulation, strengthens steadily during its development, and then weakens as it dissipates. The connector vortex shows a more pronounced change in net rotational strength mainly during its decay phase, coinciding with a reduction in vortex area. The clockwise-oriented hub vortex shows a gradual decrease in circulation magnitude over its approximately 4 minute detected lifetime, while its boundary undergoes noticeable fluctuations.

Panel (g) shows a subset of vortices detected over a ≈7 minute interval, with the peripheral, connector, and hub vortices highlighted in blue, black, and purple, respectively. The presented examples suggest that unclassified vortices are typically shorter-lived, whereas vortices belonging to one of the three classes tend to persist for longer durations, consistent with the statistical trends shown in Figure 3(d) and Figure C1.

Longer-lived vortices may exert a greater cumulative influence on the surrounding plasma simply because they remain coherent for longer. Photospheric vortices have been proposed as seeds for vortex tubes that extend into higher atmospheric layers and may facilitate energy flow into the chromosphere and corona (S. Shelyag et al. 2011; S. Wedemeyer-Böhm et al. 2012; C. A. Breu et al. 2023). In this context, peripheral, connector, and hub vortices, which remain coherent for longer than the typical vortex in our sample, could contribute more significantly to upward energy transport. However, quantifying this contribution requires a direct energy flux analysis.

Role classes likely also describe how a vortex is coupled to its environment and that coupling can directly affect how long a vortex remains detectable and coherent. This coupling can help determine the balance between processes that generate or maintain a vortex and processes that promote decay (K. Tziotziou et al. 2023). Each role has different characteristics that are defined

in terms of vortex interaction; however, these differences often also have implications for where the vortex sits relative to other vortices and therefore for which processes are likely to dominate the local flow (M. Gopalakrishnan Meena & K. Taira 2021).

Peripheral vortices tend to occupy spatially isolated communities, shielding them from disruptive interactions and strain from neighboring groups. Connectors are more spatially central, exposing them to ongoing interactions that may help regenerate and sustain them. Hub vortices, defined by the largest total induced velocity output, likely combine strong circulation with a central position, benefiting from similar ongoing driving. A hub's larger size and stronger circulation make it harder to disrupt, potentially contributing to a longer detectable lifetime. Connector vortices may persist for analogous reasons. We note that our results reflect continued detection, so vortices maintaining a sufficiently strong circulatory strength may do so partly because their network role and spatial positioning provide a more stable dynamical environment.

3.2. Photospheric–Chromospheric Vortex Tubes

Following the vortex lifetime analysis, we also examine the vertical persistence of vortices, measuring how far they extend from the photosphere into the chromosphere before dissipating. We define dissipation as the absence of a local detection in the next horizontal layer. The analysis uses the full horizontal field of view and spans a vertical extent of ≈1.55 Mm. We track vortex tubes rooted at the top of the photosphere (≈0.45 Mm) over ≈37 minutes of solar time. Across this interval, we detect and track more than 5100 vortex tubes, from rotational vortical structures confined to the photosphere to those extending into the chromosphere. Moreover, each vortex tube contributes one tube length measurement to the statistics of its assigned class, even if it is detected across multiple discrete z heights. We assign the peripheral, connector, or hub label at the photospheric base layer and retain this label when tracking the tube's vertical extent. The class labels shown in Figure 3 and the mean values reported here therefore refer to the base layer classification.

Figure 3(e) shows the distribution of vortex tube lengths with a mean tube length equal to 0.16 Mm. The full distribution is right skewed, indicating that most tubes are short. When we restrict the sample to hub vortices (see bottom panel of Figure C2), the distribution becomes broader, consistent with their larger mean tube length of 0.35 Mm. Peripheral and connector vortices also have longer mean lengths of 0.20 and 0.26 Mm, respectively, compared with 0.16 Mm for all detected vortices (see also Figure C2).

Vortex tubes that remain detected at the highest height considered (≈2 Mm) are excluded from Figure 3(e) and from the mean values in this section, since their full lengths are not observed within the analyzed range. Out of the 255 vortices that persist to the final vertical extent, the numbers of which are part of the highlighted groups are 21 peripheral, 28 connector, and 52 hub vortices, each exceeding 1.5 Mm in length. We exclude these cases to avoid skewing the distribution and to ensure the reported statistics fully reflect observed tube lengths.

Tiles (d), (e), (f), and (h) in Figure 4 show examples of Γ detected vortex tubes. We plot the vortex boundaries and centers at each height where the tube is detected. The boundary color indicates circulation at each height and therefore shows how the net rotational strength varies along the vertical extent. Vortex (d) is a peripheral vortex that strengthens near the base and maintains relatively high circulation up to its final detected height of ≈2 Mm. The hub vortex (f) shows a similar evolution but with a shorter detected height of around 0.6 Mm. Of the three examples, the connector vortex (e) is the longest, reaching ≈1 Mm. It has lower circulation in the lower half of the tube, before strengthening as the boundary expands. Toward the upper end of vortex (e), both the boundary size and circulation decrease until the vortex is no longer detected. Across the three classes, hub vortices generally show the largest net rotational strength.

Panel (h) in Figure 4 shows a subset of detected vortex tubes, with the peripheral, connector, and hub examples highlighted in blue, black, and purple. In this subset, the two tubes with the greatest vertical extents are classified as peripheral or hub. While Figures 3 and 4 differ in what they summarize, both evidence that vortices assigned to one of the three classes are more likely to persist to greater heights than unclassified vortices, with the effect most pronounced for hub vortices.

3.3. Global Trajectories of Vortex Communities

Vortex communities evolve, and their membership changes, vortices move, and circulation varies, all influencing the inferred community position. To quantify community location and motion, we assign each community a representative center. The centroid of a community is defined as the circulation weighted spatial average of its member vortices (M. Gopalakrishnan Meena et al. 2018; M. Gopalakrishnan Meena & K. Taira 2021):

$$\boldsymbol{c}_i = \frac{\sum_{j\in C_i} |\gamma_j| \boldsymbol{r}_j}{\sum_{j\in C_i} |\gamma_j|}. \tag{4}$$

The weight is the absolute circulation $|\gamma_j|$. Here, C_i denotes community i and $\boldsymbol{r}_j$ is the position of vortex j.

We infer community motion by tracking centroid positions for coherent vortex communities across the full time interval (between successive 10 s frames) and field of view described in Section 2.1, evaluated at a photospheric height of ≈0.45 Mm. Community motion is classified using three trajectory metrics: net displacement, total displacement, and turning behavior. We define E as the ratio of net displacement to total displacement and $\bar{\theta}$ as the mean angle between successive displacement vectors and use them to classify the resulting trajectories into four types: helical, kinked, directed, and no pattern. Directed trajectories are defined by $E \geqslant 0.9$, kinked trajectories by $\bar{\theta} > 1.5$ rad, and helical trajectories by $E < 0.4$ and $\sum\theta > 4\pi$ (with θ in radians). Communities that do not satisfy any criterion are assigned to the no-pattern class. Figure 5 shows examples of each class. Helical trajectories exhibit swirling motion ((b), (c), (f), and (g)), kinked trajectories show abrupt changes in direction (e), and directed trajectories follow a smooth, coherent path (d). Trajectories that do not match these behaviors are grouped as no pattern and show no consistent structure (a).

Table 1 summarizes the prevalence of the different centroid motion types exhibited by vortex communities. Classification requires at least four detected frames, corresponding to a 40 s trajectory. Longer-lived communities (⩾1.5 minutes), which contain nine or more position vectors, provide a clearer

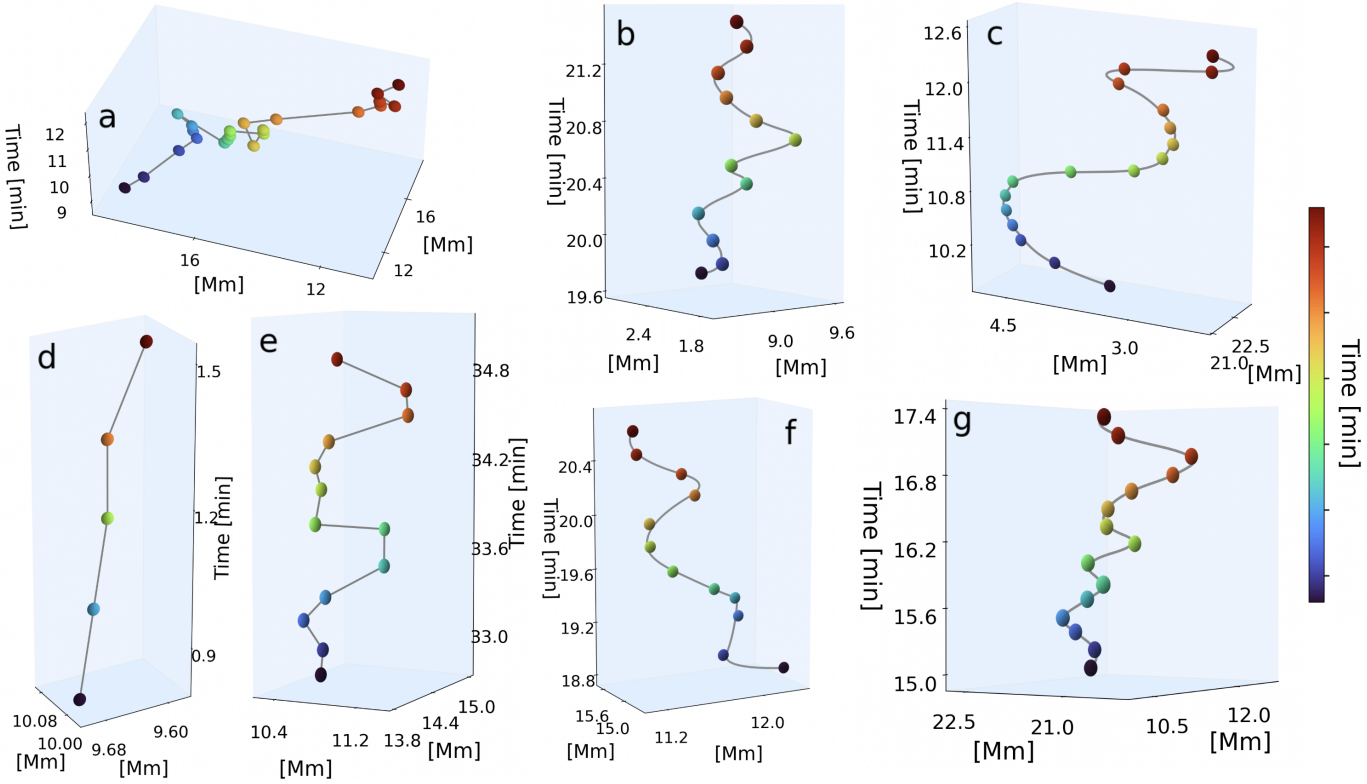


Figure 5. Community centroid trajectories over time in a fixed horizontal plane. Panels (b), (c), (f), and (g) show four examples exhibiting helical motion, while panels (d) and (e) show examples of directed and kinked motion, respectively. Finally, panel (a) shows an unclassified centroid trajectory, exhibiting no clear motion pattern. Spheres denote centroid positions and are colored by time.

Table 1
The Types of Trajectories Exhibited by Community Centroids

Minimum Community Lifetime	Helical	No Pattern	Kinked	Directed	Quantity
4 Frames	36.4%	34.1%	20.2%	9.3%	129
5 Frames	39.8%	34.7%	18.6%	6.8%	118
6 Frames	48.5%	33.0%	14.4%	4.1%	97
7 Frames	51.1%	33.7%	14.1%	1.1%	92
8 Frames	54.0%	31.0%	14.9%	0.0%	87
9 Frames	59.5%	27.9%	12.7%	0.0%	79

Note. For each row, we only consider communities that persist for at least x frames. The column labeled quantity indicates the number of communities within that "minimum lifetime" defined group.

measure of global motion and support more robust categorization. Because these longer-lived communities persist for longer, they may also be more dynamically relevant. We therefore repeat the analysis using minimum length thresholds of 4–9 frames and report the resulting motion-type proportions and total communities tracked after excluding communities shorter than each threshold. As expected, the number of identified communities decreases as the minimum lifetime threshold is increased. However, even when restricting the analysis to communities with lifetimes of $\geqslant$1.5 minutes, 79 community trajectories remain available for analysis.

Directed vortex groups are rare in our dataset, with proportions between 0% and 9.3%. Persistently unidirectional centroid motion is mostly confined to short-lived communities, and straight-line trajectories are uncommon overall. Kinked vortex groups occur more frequently (12.7%–20.2%) but remain a minority class. Kinked motion is most prevalent when short-lived communities are included, but it is still observed when restricting the sample to longer-lived communities.

We next consider centroid trajectories that may reflect a net vortical motion. For point vortices, groups of idealized vortices can generate helical motion in the induced flow field (P. G. Saffman 1992). Our results are consistent with similar behavior occurring for solar vortex communities. Table 1 shows helical classification rates of 36.4%–59.5%, with higher rates among longer-lived communities. The no-pattern class remains substantial (27.9%–34.7%), which could arise from strict classification thresholds and/or from communities with weaker intracommunity interactions that do not produce a clear centroid motion signature.

4. Discussion and Conclusion

In this work, we use a community detection algorithm to analyze photospheric vortices as an interacting system rather than isolated features. We analyzed 37 minutes of Bifrost simulation and tracked vortices through their spatial and temporal extent. We use the reduced network, constructed from interaction strengths defined via the Biot–Savart induced velocity, to identify key structures within the system (P. G. Saffman 1992; A. G. Nair & K. Taira 2015; M. Gopalakrishnan Meena et al. 2018). We identified 340 distinct communities, with an average size of 3 spanning an average of 1.12 minutes.

Vortices are categorized according to their role within the interaction network as peripheral, connector, or hub nodes (M. Gopalakrishnan Meena & K. Taira 2021). These roles describe dynamical influence: peripheral vortices act mainly

within their community, connectors link communities, and hubs have the greatest total outgoing induced velocity strength. Vortex tube lengths and lifetimes of fully observed vortices classified as peripheral, connector and hub are larger than those of the full vortex population, which is consistent with these vortices persisting to greater heights and remaining coherent for longer (I. N. Kitiashvili et al. 2012; S. S. A. Silva et al. 2020). Vortices with longer lifetimes and vertical extents are expected to have a larger cumulative influence on photospheric and chromospheric dynamics (S. S. A. Silva et al. 2024a).

The network-based framework reveals coherent, large-scale structures that are not apparent from individual vortex detections alone (M. Gopalakrishnan Meena et al. 2018; M. Gopalakrishnan Meena & K. Taira 2021). The centroid trajectories of these communities capture collective dynamics that extend beyond the motion of their constituent vortices, with a substantial fraction exhibiting signatures consistent with net vortical drift, exemplified in Figure 5. While analogous helical motion can be demonstrated for idealized point-vortex systems, establishing such behavior rigorously in turbulent magnetohydrodynamic regimes remains challenging (P. G. Saffman 1992; Y. Fukumoto & V. L. Okulov 2005). Nevertheless, 36.4%–59.5% of the detected communities are classified as helical, supporting the interpretation that vortex collectives may sustain global rotational dynamics and thereby enhance their capacity to excite waves (V. Fedun et al. 2011; K. Tziotziou et al. 2023), moving beyond localized wave drivers.

Acknowledgments

L.M. is grateful for the STFC studentship. V.F., G.V., I.B., and S.S.A.S. are grateful to The Royal Society, International Exchanges Scheme, collaboration with Greece (IES/R1/221095), India (IES/R1/211123), and Taiwan (IEC/R3/233017). V.F., G.V., and S.S.A.S. are grateful to the Science and Technology Facilities Council (STFC) grants ST/V000977/1, ST/Y001532/1, and UKRI1165. S.S.A.S. and V.F. would like to thank the International Space Science Institute (ISSI) in Bern, Switzerland, for the hospitality provided to the members of the team on "The Nature and Physics of Vortex Flows in Solar Plasmas" and "Tracking Plasma Flows in the Sun's Photosphere and Chromosphere: A Review & Community Guide." L.M. is grateful to Sue Knight for all of her ongoing support.

Appendix A
Vortex Detection

A.1. The Gamma Method

The Γ method of L. Graftieaux et al. (2001) provides an automated approach to identify vortex centers and boundaries from particle image velocimetry velocity fields. This is valuable for astrophysical datasets because it scales well to large simulation and observational volumes and can be applied across a broad range of spatial scales. The method is well established in the wider fluids literature, including terrestrial and space-based applications, and is commonly used in turbulent regimes where distinguishing shear from rotation is important. The two top panels of Figure 2 (tiles (a)–(g)) show examples of Γ detected vortices. The streamlines indicate that the detected boundaries and centers coincide with locally rotating flow.

The method relies on two complementary functions: Γ_1, which identifies the vortex center, and Γ_2, which detects the vortex boundary. For a given point P, these functions are defined in the discrete framework as follows:

$$\Gamma_1(P) = \frac{1}{N}\sum_S \frac{[\boldsymbol{PM} \times \boldsymbol{U}_M] \cdot \boldsymbol{z}}{\|\boldsymbol{PM}\| \cdot \|\boldsymbol{U}_M\|} = \frac{1}{N}\sum_S \sin(\theta_M), \tag{A1}$$

$$\Gamma_2(P) = \frac{1}{N}\sum_S \frac{[\boldsymbol{PM} \times (\boldsymbol{U}_M - \tilde{\boldsymbol{U}}_P)] \cdot \boldsymbol{z}}{\|\boldsymbol{PM}\| \cdot \|\boldsymbol{U}_M - \tilde{\boldsymbol{U}}_P\|}. \tag{A2}$$

Here, the functions are evaluated over a local kernel S containing N discrete points, where M denotes a point in S. The velocity at point M is denoted by $\boldsymbol{U}_M$, while $\tilde{\boldsymbol{U}}_P$ is the local convection velocity around point P, defined as

$$\tilde{\boldsymbol{U}}_P = \frac{1}{N}\sum_{M\in S} \boldsymbol{U}_M. \tag{A3}$$

In this context, $\boldsymbol{z}$ is the unit vector normal to the measurement plane, $\boldsymbol{PM}$ is the vector from point P to point M, and θ_M is the angle between $\boldsymbol{PM}$ and $\boldsymbol{U}_M$.

The functions Γ_1 and Γ_2 are based on local flow topology. This makes them less sensitive to absolute velocity magnitude and helps suppress small-scale turbulent fluctuations. Using user-defined thresholds, the method identifies candidate vortex centers and boundaries. A detection is recorded only when a Γ_1 center lies within a Γ_2 boundary and when the absolute values exceed the chosen thresholds $\Gamma_{1_{\rm Thr}}$ and $\Gamma_{2_{\rm Thr}}$:

$$|\Gamma_1| > \Gamma_{1_{\rm Thr}} \quad \text{and} \quad |\Gamma_2| > \Gamma_{2_{\rm Thr}}.$$

Large magnitudes of Γ_1 and Γ_2 (both bounded in $[-1, 1]$) are associated with rotational flow, while the sign indicates the orientation of rotation.

Here, we use adaptive thresholding to better capture vortices during decay, when their rotational signature can weaken. In these phases, fixed threshold methods can miss detections and truncate lifetimes. Our dual aspect approach is designed to reduce this effect and support more consistent tracking through a vortex lifetime.

A.2. The Dual-part Gamma Method

The dual-part Γ method builds on the original Γ framework and uses the same Γ_1 and Γ_2 functions but changes how they are applied during tracking. The key idea is to vary threshold values dynamically when following vortex evolution in time and height. In regions that were previously flagged as detections, we lower the Γ_1 threshold to support continued identification of the same vortex through weaker phases of its lifetime and vertical extent. In regions with no prior detection, we keep Γ_1 higher to reduce false positives. We use an initial threshold of 0.75, and when a previous detection exists, we reduce it to 0.64 ($2/\pi$).

For boundary identification, we fix $\Gamma_{2_{\rm Thr}} = 2/\pi$ for both initial and subsequent detections. This follows L. Graftieaux et al. (2001), who showed that in the limit $S \to 0$, regions with $|\Gamma_2| > 2/\pi$ are rotation dominated rather than dominated by shear or strain. Keeping the boundary threshold constant helps keep the detected vortex area comparable over time, aside from physical changes during vortex evolution. Given that our calculations for circulation and thus induced velocity are based upon the boundary of the vortex, the constant boundary

threshold is particularly important in this work. It ensures consistency in circulation estimates across the considered vortices, creating a more reliable progression of vortex community detections.

A.3. Normalization as a Preprocessing Step

Robust vortex detection is central to our analysis. To improve the boundary estimates, we apply a normalization preprocessing step to the horizontal velocity field and compute the Γ fields from this normalized field. This removes sensitivity to velocity magnitude and emphasizes flow topology, which can lead to more consistent vortex boundaries. In particular, this step produces more convex boundaries (L. McClure et al. 2026), which have been used as an indicator of more reliable vortex identification (G. Haller et al. 2016; K. Tziotziou et al. 2023).

Appendix B
Peripheral, Connector, and Hub Definitions

In this paper, we use the peripheral, connector, and hub definitions to classify vortices (nodes) within the interaction network (M. Gopalakrishnan Meena & K. Taira 2021). The characteristic properties of these structures are described in Section 2.2. These classes are defined relative to the reduced network structure and, therefore, relative to the inferred vortex interaction strengths.

Hub nodes are characterized by a large total outward inducing strength (M. Gopalakrishnan Meena & K. Taira 2021). For vortex i, we define

$$s_i = \sum_{j \neq i} u_{i \to j}. \tag{B1}$$

In our analysis, we identify a single hub node, defined as the vortex with the maximum outward inducing strength, $i_{\text{hub}} = \arg\max_i s_i$.

Peripheral and connector nodes are identified using community structure by comparing how strongly a vortex interacts within its assigned community versus outside it. For a vortex i in community k, we define the intracommunity interaction strength as

$$s_i^{\text{intra}} = \sum_{j \in C_k} \sum_{j \neq i} u_{i \to j} \tag{B2}$$

and the intercommunity interaction strength as

$$s_i^{\text{inter}} = \sum_{j \notin C_k} u_{i \to j} \tag{B3}$$

(M. Gopalakrishnan Meena & K. Taira 2021). These quantities quantify the relative influence of a vortex on its own community compared to the rest of the network. The balance between s_i^{intra} and s_i^{inter} varies between vortices depending on their circulation and spatial distribution.

We introduce a within-module Z score to quantify the relative intracommunity interaction strength of a vortex within its assigned group (M. Gopalakrishnan Meena & K. Taira 2021). For a vortex i, this is defined as

$$Z_i = \frac{s_i^{\text{intra}} - \overline{s^{\text{intra}}}_k}{\sigma_{s_k^{\text{intra}}}}. \tag{B4}$$

Here, $\overline{s^{\text{intra}}}_k$ and $\sigma_{s_k^{\text{intra}}}$ are the mean and standard deviation of s^{intra} computed over all vortices in the community k to which vortex i belongs.

Finally, we introduce a participation coefficient, P, to quantify how a vortex's intercommunity influence is distributed across the network (M. Gopalakrishnan Meena & K. Taira 2021). This measures how evenly a vortex spreads its interaction strength across communities. With $P \in [0, 1]$, its high values indicate that a vortex's influence is distributed relatively evenly across communities, whereas the low values indicate that its influence is concentrated mainly within its assigned community. For a vortex i in community k,

$$P_i = 1 - \left[\left(\frac{s_i^{\text{intra}}}{s_i} \right)^2 + \sum_{j \notin C_k} \left(\frac{u_{i \to j}}{s_i} \right)^2 \right]. \tag{B5}$$

For each community k, both the peripheral and connector vortices are selected as the vortex with the largest within-module Z score, i.e., $\max_{i,, i \in C_k} Z_i$. The distinction between peripheral and connector then depends on how strongly the community interacts with the rest of the network. We define the peripheral vortex as the Z-maximizing vortex in the community with the smallest mean participation coefficient, $\min_k \overline{P_k}$, and the connector vortex as the Z-maximizing vortex in the community with the largest mean participation coefficient, $\max_k \overline{P_k}$ (M. Gopalakrishnan Meena & K. Taira 2021). Here, $\overline{P_k}$ is the mean value of P across all vortices in the community k.

In the solar context, where large domains can be sparsely populated, the optimal network partition can include single vortex communities. For these communities $s^{\text{intra}} = 0$, s^{inter} is typically small and have undefined Z. We treat these cases as isolated communities and exclude them from the peripheral, connector, and hub classification.

Appendix C
Properties of Peripheral, Connector, and Hub Vortices

In Sections 3.1 and 3.2 we show that on average the three classes of vortices (peripherals, connectors, and hubs) persist further in the z-direction from photospheric heights and also have longer detectable lifespans. We present the time and length distributions for each class in Figures C1 and C2, respectively. Each figure shows the smoothed probability density distribution for each class with the probability density distribution for the entire dataset as a histogram in the background.

Compared with whole population distributions, which are strongly concentrated at short lifetimes and small vertical lengths, the smoothed role-based distributions are broader and shifted toward larger values. In Figure C1, the peripheral and connector populations show similar lifetime distributions, whereas hubs peak at longer lifetimes and display the largest mean and a pronounced extended tail. In Figure C2, we see the same progression is present for vertical length: peripheral vortices remain weighted toward smaller lengths, connectors extend somewhat higher, and hubs have the broadest distribution and greatest average vertical extent. Overall, vortices assigned a network role, particularly hubs, tend to persist for longer and extend farther vertically than the general vortex population.

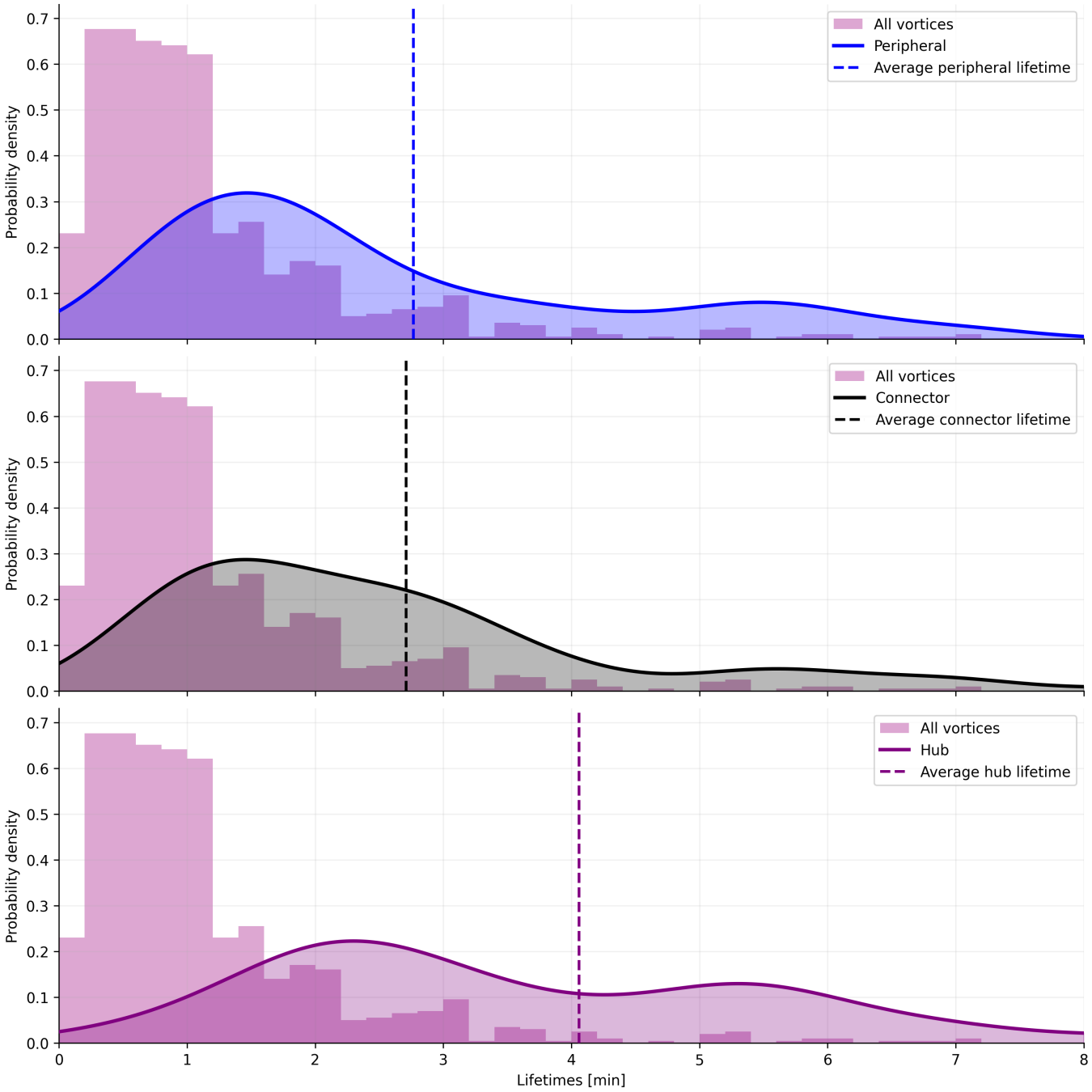


Figure C1. Probability density distributions of the lifetimes of peripheral (top), connector (middle), and hub (bottom) vortices. The pink histograms show the distribution for all vortices (see also panel (d) of Figure 3), while the solid curves and corresponding shaded regions show the smoothed distributions for each network role. Dashed vertical lines indicate the mean lifetime of each role.

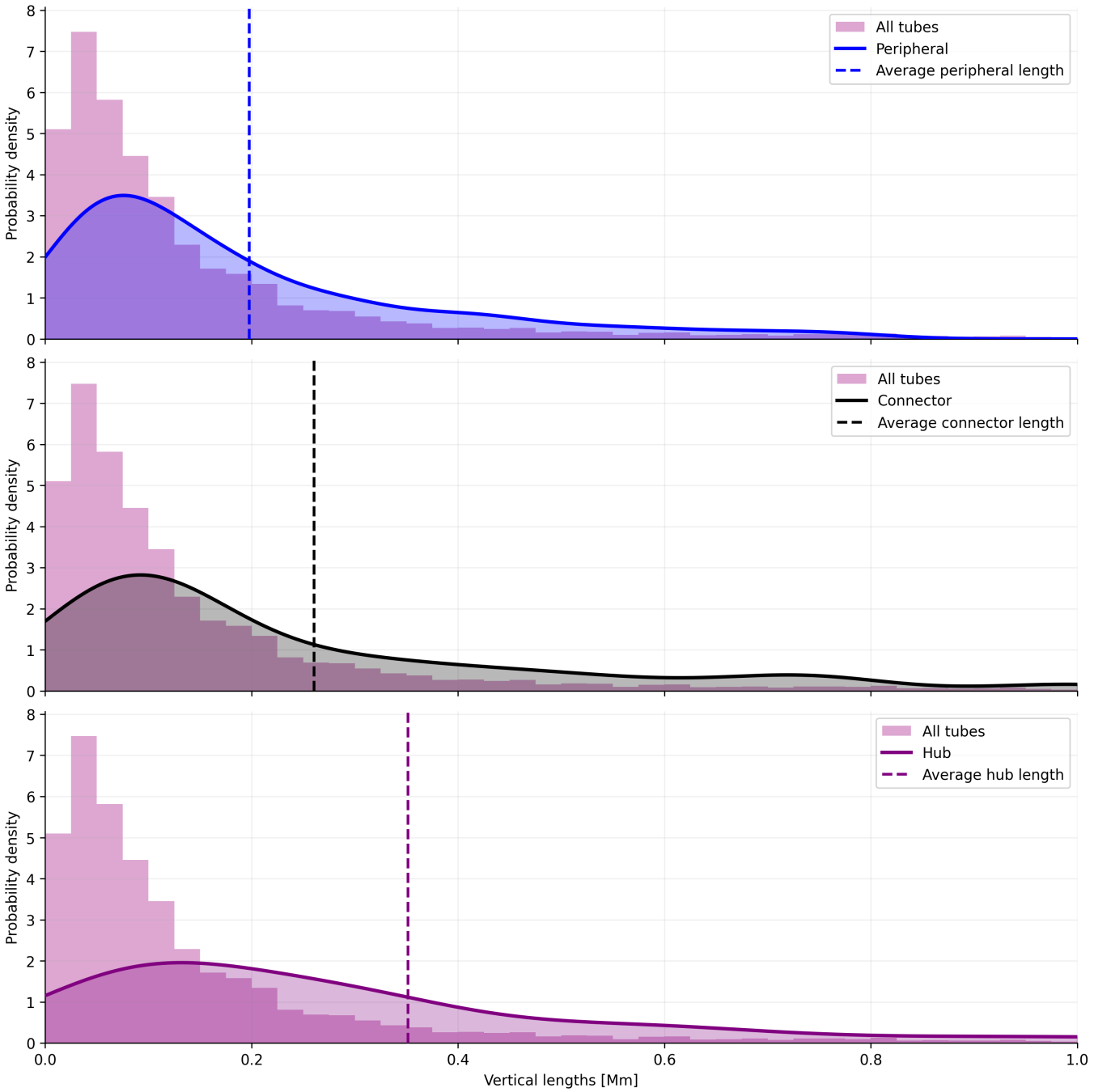


Figure C2. Probability density distributions of the vertical lengths of peripheral (top), connector (middle), and hub (bottom) vortices. The pale-pink histograms show the distribution for all vortices (see also panel (e) of Figure 3), while the solid curves and corresponding shaded regions show the smoothed distributions for each network role. Dashed vertical lines mark the mean vertical length of each role.

ORCID iDs

Lauren McClure https://orcid.org/0009-0000-4129-1324
Suzana Silva https://orcid.org/0000-0001-5414-0197
Gary Verth https://orcid.org/0000-0002-9546-2368
Istvan Ballai https://orcid.org/0000-0002-3066-7653
Viktor Fedun https://orcid.org/0000-0002-0893-7346

References

Aljohani, Y., Fedun, V., Ballai, I., et al. 2022, ApJ, 928, 3
Bassett, D. S., Wymbs, N. F., Porter, M. A., et al. 2011, PNAS, 108, 7641
Blondel, V. D., Guillaume, J.-L., Lambiotte, R., & Lefebvre, E. 2008, JSMTE, 2008, P10008
Breu, C. A., Peter, H., Cameron, R., & Solanki, S. K. 2023, A&A, 675, A94
Cabral, B., & Leedom, L. C. 1993, Proc. of the 20th Annual Conf. on Computer Graphics and Interactive Techniques, 263
Carlsson, M., Hansteen, V. H., Gudiksen, B. V., Leenaarts, J., & De Pontieu, B. 2016, A&A, 585, A4
Fedun, V., Shelyag, S., Verth, G., Mathioudakis, M., & Erdélyi, R. 2011, AnGeo, 29, 1029
Finley, A., Brun, A., Carlsson, M., et al. 2022, A&A, 665, A118
Fukumoto, Y., & Okulov, V. L. 2005, PhFl, 17, 107101
Giagkiozis, I., Fedun, V., Scullion, E., Jess, D. B., & Verth, G. 2018, ApJ, 869, 169
Gopalakrishnan Meena, M., Nair, A. G., & Taira, K. 2018, PhRvE, 97, 063103

Gopalakrishnan Meena, M., & Taira, K. 2021, JFM, 915, A10
Graftieaux, L., Michard, M., & Grosjean, N. 2001, MeScT, 12, 1422
Gudiksen, B. V., Carlsson, M., Hansteen, V. H., et al. 2011, A&A, 531, A154
Haller, G., Hadjighasem, A., Farazmand, M., & Huhn, F. 2016, JFM, 795, 136
Kitiashvili, I. N., Kosovichev, A. G., Mansour, N. N., & Wray, A. A. 2012, ApJL, 751, L21
Kuniyoshi, H., Imada, S., & Yokoyama, T. 2025, ApJL, 990, L71
Kuniyoshi, H., Shoda, M., Iijima, H., & Yokoyama, T. 2023, ApJ, 949, 8
Lewis, A. C. F., Jones, N. S., Porter, M. A., & Deane, C. M. 2010, BMC Systems Biology, 4, 100
MacMahon, M., & Garlaschelli, D. 2015, PhRvX, 5, 021006
McClure, L., Silva, S., Verth, G., Ballai, I., & Fedun, V. 2026, ApJ, 1002, 58
Moll, R., Cameron, R. H., & Schüssler, M. 2011, A&A, 533, A126
Nair, A. G., & Taira, K. 2015, JFM, 768, 549
Newman, M. 2010, Networks: An Introduction (Oxford Univ. Press)
Newman, M. E. J. 2006, PNAS, 103, 8577
Newman, M. E. J., & Girvan, M. 2004, PhRvE, 69, 026113
Priest, E. 2014, Magnetohydrodynamics of the Sun (Cambridge Univ. Press)
Saffman, P. G. 1992, Vortex Dynamics (Cambridge Univ. Press)
Shelyag, S., Fedun, V., Keenan, F. P., Erdélyi, R., & Mathioudakis, M. 2011, AnGeo, 29, 883
Silva, S. S. A., Fedun, V., Verth, G., Rempel, E. L., & Shelyag, S. 2020, ApJ, 898, 137
Silva, S. S. A., Verth, G., Ballai, I., et al. 2024a, ApJ, 975, 118
Silva, S. S. A., Verth, G., Rempel, E. L., et al. 2024b, ApJ, 963, 10
Taira, K., Nair, A. G., & Brunton, S. L. 2016, JFM, 795, R2
Tziotziou, K., Tsiropoula, G., Kontogiannis, I., Scullion, E., & Doyle, J. G. 2018, A&A, 618, A51
Tziotziou, K., Scullion, E., Shelyag, S., et al. 2023, SSRv, 219, 1
Vargas Domínguez, S., Palacios, J., Balmaceda, L., Cabello, I., & Domingo, V. 2011, MNRAS, 416, 148
Wedemeyer-Böhm, S., Scullion, E., Steiner, O., et al. 2012, Natur, 486, 505
Yadav, N., Cameron, R. H., & Solanki, S. K. 2020, ApJL, 894, L17
Zuccarello, F. P., Aulanier, G., Dudík, J., et al. 2017, ApJ, 837, 115